

Photonics-enabled broadband continuous-wave terahertz computed tomography

Zuomin Yang (杨作民), Lu Zhang (张鹿), Zhidong Lü (吕治东), Xing Fang (方兴), and Xianbin Yu (余显斌)*

College of Information Science and Electronic Engineering, Zhejiang University, Hangzhou 310027, China

*Corresponding author: xyu@zju.edu.cn

Received October 8, 2024 | Accepted December 23, 2024 | Posted Online May 16, 2025

In this paper, we propose a photonic terahertz (THz) continuous-wave computed tomography (CT) system employing an optical frequency comb and specialized imaging algorithms. Our work leverages the system to offer unique advantages in detecting and analyzing samples that are challenging for traditional 2D scanning systems. Our experimental results, operating at 330 GHz, reach an exceptionally low amplitude standard deviation of 0.016 mV. Additionally, the proposed system performs nondestructive CT detection with a 0.5 mm error margin and obtains enhanced image quality, showing its great promise for implementing THz-CT imaging with high robustness and resolution.

Keywords: photonic terahertz; computed tomography; nondestructive detection; imaging.

DOI: [10.3788/COL202523.063901](https://doi.org/10.3788/COL202523.063901)

1. Introduction

The terahertz (THz, 0.1–10 THz) wave, which has garnered increasing attention, lies between the microwave and infrared bands, and possesses several unique physical properties, including a nonionizing nature, low photon energy, good penetrability, and a distinctive fingerprint spectrum. These attributes make THz waves highly promising for applications in detection and have proven viable in fields such as medical diagnostics^[1], non-contact and nondestructive detection^[2], and water content measurement^[3]. Extensive research has focused on developing THz detection systems. For instance, Song *et al.* proposed a two-dimensional (2D) scanning THz system at 325 GHz using two-tone square-law detection^[4], achieving vector imaging and an amplitude standard deviation of 0.23 mV. Similarly, Cao *et al.* demonstrated a comparable THz imaging system at 300 GHz^[5] that reached an amplitude standard deviation of 0.13 mV. In contrast, Dülme *et al.* reported a THz imaging system at 300 GHz that utilized a second reference photodiode to eliminate additional phase-noise terms^[6], achieving an amplitude standard deviation of approximately 0.02 mV and an ultra-low phase-noise of 0.034°. Our current work^[7], which was based on an optical frequency comb (OFC) and two-stage mixing, accomplished an amplitude standard deviation of 0.032 mV. Nevertheless, most of these systems rely on 2D mechanical scanning schemes, which limit their ability to accommodate various sample shapes and sizes, particularly sections of elongated samples. Alternatively, the THz computed tomography (CT) scheme is highly suitable for such samples, as it enables visualization of internal structures, showcasing the three-dimensional (3D) configurations of samples^[8].

However, the image quality and resolution of THz-CT cannot match those of X-ray CT due to its larger beam waist radius^[9]. Consequently, additional devices are typically required to improve detection performance^[10–12]. Moreover, sources in most previous THz-CT systems are predominantly based on continuous-wave (CW) gas lasers, frequency multipliers of Gunn tubes, or pulsed THz time-domain spectroscopy (THz-TDS)^[13–17]. These methods suffer from restricted electronic bandwidth and limited frequency tunability in CW systems, and low signal-to-noise ratio and complex signal processing in pulsed systems. In this context, photonics-enabled CW THz sources are recommended to address these challenges, demonstrating advantageous performance in imaging systems^[18].

In this paper, we propose a high-performance CT-based non-destructive detection method using the photonics-enabled THz CW scheme that incorporates custom digital algorithms. In the proof-of-concept experiment, an OFC and a unitraveling carrier photodiode are employed for THz signal generation, with a Schottky barrier diode serving as the receiver for CT detection. Detection information is extracted by a lock-in amplifier, and the original CT sinograms are processed using our specialized THz imaging algorithms. The experimental nondestructive CT demonstration exhibits stable performance over 24 h, achieving a 0.5 mm error margin and enhanced image quality without additional devices.

2. Methods

The experimental setup of the proposed scheme is illustrated in Fig. 1. A laser (NKT) emits a 16 dBm optical signal at

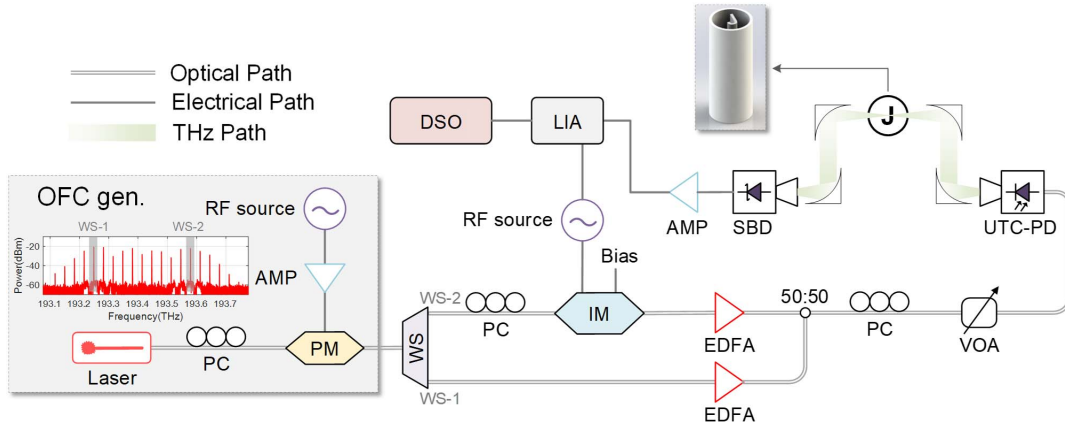


Fig. 1. Experimental setup of the photonic THz-CT system. PC, polarization controller; RF, radio-frequency; AMP, amplifier; PM, phase modulator; WS, wave shaper; IM, intensity modulator; EDFA, erbium-doped fiber amplifier; VOA, variable optical attenuator; UTC-PD, untraveling-carrier photodiode; SBD, Schottky barrier diode; LIA, lock-in amplifier; DSO, data storage oscilloscope. The inset shows the optical spectrum of OFC after the PM.

193.414 THz. A phase modulator (PM, EOSPACE) driven by a 33 GHz amplified radio-frequency (RF) signal with a power of 25 dBm generates an OFC. Subsequently, a wave shaper (WS, Finisar) filters out two optical frequency components at 193.249 and 193.579 THz, serving as the optical local oscillator (LO) and carrier, respectively. The spectrum of the OFC and the WS selection is depicted in the inset of Fig. 1. By adjusting the line spacing of the OFC and selecting different orders of comb lines, different frequencies can be obtained. Please note that the photonics-enabled THz source offers an extensive tuning range, while the eventual frequency should take into account other devices' operation bandwidths in the system. A 3 MHz RF signal with a power of 12 dBm is divided into two branches. One branch modulates the optical carrier via an intensity modulator (IM, EOSPACE) operating at its linear point to generate ± 1 st harmonics, while the other serves as a reference signal for subsequent phase locking. The modulated optical signal and the optical LO are power-balanced by erbium-doped fiber amplifiers (EDFAs), coupled, and launched into a untraveling carrier photodiode (UTC-PD, PMAN-13001, NTT) to generate THz waves at 329.997, 330, and 330.003 GHz, which radiate into the air via a horn antenna. Since the UTC-PD is a polarization-sensitive device, different polarization states of the input optical signal can lead to varying optoelectronic conversion efficiencies. To maximize the utilization of the input optical signal's power and increase the conversion efficiency, it is necessary to use a polarization controller (PC) to adjust the polarization state of the optical signal before it enters the UTC-PD^[19].

In the free-space stage, two parabolic mirrors (GCC-501101, DHC) focus the THz waves onto a sample, and two additional parabolic mirrors collimate the THz waves toward a receiving antenna.

Regarding reception, the THz waves are converted into electrical signals at 3 and 6 MHz in a Schottky barrier diode (SBD, VDI) through self-mixing. The sample information is embedded within the output amplitude of the SBD. These

signals are then amplified by intermediate frequency amplifiers (AMPs, SHF804B) with a gain of 44 dB. A lock-in amplifier (LIA, Zurich Instruments) extracts the sample information from the 3 MHz signal.

In the experiment, continuous line scans are conducted by moving the sample through the THz focus at a velocity of 28.13 mm/s with steps of 5 mm. After each line scan, the sample is rotated by 1 deg until a full 360-deg scan is completed. The total acquisition time is approximately 30 min, primarily constrained by the motor speeds and the number of transceivers.

We assume that the output of the laser is

$$E_l(t) = A_l \exp\{j\{\omega_l + \omega_{nl}(t)t + \varphi_{nl}(t)\}\}, \quad (1)$$

where A_l and ω_l are the amplitude and angular frequency of the laser, and $\omega_{nl}(t)$ and $\varphi_{nl}(t)$ denote the angular frequency fluctuation and phase noise of the laser, respectively. After the modulation, we choose two components of the OFC as the optical carrier and LO, which can be given as

$$E_c(t) = A_c \exp\{j\{\omega_c + \omega_{nl}(t)t + \varphi_{nl}(t)\}\}, \quad (2)$$

$$E_{LO}(t) = A_{LO} \exp\{j\{\omega_{LO} + \omega_{nl}(t)t + \varphi_{nl}(t)\}\}, \quad (3)$$

where A_c , A_{LO} , ω_c , and ω_{LO} are the amplitudes and angular frequencies of the optical carrier and LO, respectively. Then, the optical carrier is modulated by the RF signal through the IM to generate harmonics, which can be expressed as

$$E_{IM}(t) = A_c \left\{ J_0 \left(\frac{\pi V_m}{2V_\pi} \right) \cdot \exp\{j\{\omega_c + \omega_{nl}(t)t + \varphi_{nl}(t)\}\} \right. \\ \left. + J_1 \left(\frac{\pi V_m}{2V_\pi} \right) \cdot \exp\{j\{\omega_c + \omega_{nl}(t) + \Delta\omega\}t + \varphi_{nl}(t)\}\} \right. \\ \left. + J_{-1} \left(\frac{\pi V_m}{2V_\pi} \right) \cdot \exp\{j\{\omega_c + \omega_{nl}(t) - \Delta\omega\}t + \varphi_{nl}(t)\}\} \right\}, \quad (4)$$

where $J_x(\pi V_m/2V_\pi)$ is the Bessel function of the order x , V_π is the half-wave voltage of the IM, and V_m and $\Delta\omega$ are the amplitude and angular frequency of the RF source, respectively. $\Delta\omega$ can be considered as constant, since the fluctuation of the commercial RF source is negligible compared to the optical source. Higher-order frequency components are also neglected here because of very small amplitudes. Then the signals are combined with the optical LO and injected into the UTC-PD. In this case, the angular frequency fluctuation $\omega_{nl}(t)$ and the phase noise $\varphi_{nl}(t)$ of the laser in signals can be eliminated through heterodyning, and the THz signals passing through the sample can be described as

$$E_{\text{THz}}(t) = A_{T1} \exp\{j[(\omega_c - \omega_{l0})t + \Phi_1]\} + A_{T2} \exp\{j[(\omega_c + \Delta\omega - \omega_{l0})t + \Phi_2]\} + A_{T3} \exp\{j[(\omega_c - \Delta\omega - \omega_{l0})t + \Phi_3]\}, \quad (5)$$

where A_{Tx} and Φ_x represent frequency-dependent attenuated amplitudes and phase shifts of the three THz components, respectively. Since $\Delta\omega$ is quite small and the ± 1 st harmonics are symmetric, we can get $\Phi_1 \approx \Phi_2 \approx \Phi_3$ and $A_{T2} \approx A_{T3}$. Subsequently, the signal is detected and self-mixed by the SBD, and the output can be expressed as

$$E_{\text{SBD}}(t) = A_{\text{DC}} + A_{T1}A_{T2} \exp[j(\Delta\omega \cdot t + \Phi_2 - \Phi_1)] + A_{T1}A_{T3} \exp[j(\Delta\omega \cdot t + \Phi_3 - \Phi_1)] + A_{T2}A_{T3} \exp[j(2\Delta\omega \cdot t + \Phi_3 - \Phi_2)] \approx A_{\text{DC}} + 2A_{T1}A_{T2} \exp[j(\Delta\omega \cdot t)] + A_{T2}A_{T3} \exp[j(2\Delta\omega \cdot t)], \quad (6)$$

where A_{DC} denotes the direct current (DC) component. As shown in Eq. (6), the information of the sample is within the amplitude of the SBD output, which can be extracted using the LIA.

To eliminate internal blur and noise while preserving the edges of the original sinograms, a THz-CT system requires additional image processing to address the issues arising from the larger focus.

- 1) First, preprocessing is crucial for the removal of salt and pepper noise; otherwise, the noise will have a devastating impact on the results of CT detection. We employ a median filter to carry out the initial filtering^[20].
- 2) Second, the sinograms obtained by the THz-CT have blurred edges, which need to be sharpened to enhance the edge sharpness. We utilize the Sobel operator for edge sharpening, as it offers precise edge localization^[21]. The sharpening can be described as

$$G_x = \begin{bmatrix} -1 & 0 & 1 \\ -2 & 0 & 2 \\ -1 & 0 & 1 \end{bmatrix} * A, \quad G_y = \begin{bmatrix} -1 & -2 & -1 \\ 0 & 0 & 0 \\ 1 & 2 & 1 \end{bmatrix} * A, \\ G = \sqrt{G_x^2 + G_y^2} \approx |G_x| + |G_y|, \\ A' = A + \alpha G, \quad (7)$$

where “*” denotes convolution, G_x and G_y , respectively, represent the edges of the original sinogram A extracted from the horizontal and vertical directions, and α ($\alpha \geq 0$) is the sharpening coefficient.

- 3) After sharpening, a bilateral filter is used to filter noise while preserving the edges^[22]. We assume the weights of pixel value (r) and spatial distance (s) are

$$G_r(p) = \exp\left(-\frac{\|I_p - I_q\|^2}{2\sigma_r^2}\right), \quad (8)$$

$$G_s(p) = \exp\left(-\frac{\|p - q\|^2}{2\sigma_s^2}\right), \quad (9)$$

where I_x denotes the value of pixel x , q is the center of the filter window, and σ represents the standard deviation. The bilateral filter can be expressed as

$$\text{BF} = \frac{1}{W_q} \sum_{p \in S} G_s(p) G_r(p) * I_p \\ = \frac{1}{W_q} \sum_{p \in S} \exp\left(-\frac{\|p - q\|^2}{2\sigma_s^2}\right) \exp\left(-\frac{\|I_p - I_q\|^2}{2\sigma_r^2}\right) * I_p, \quad (10)$$

where W_q is the weight sum of each pixel value in the filter window for normalizing the weight. W_q can be expressed as

$$W_q = \sum_{p \in S} G_s(p) G_r(p) \\ = \sum_{p \in S} \exp\left(-\frac{\|p - q\|^2}{2\sigma_s^2}\right) \exp\left(-\frac{\|I_p - I_q\|^2}{2\sigma_r^2}\right). \quad (11)$$

In flat regions, the pixel value weight G_r in the filter window is similar, making the spatial distance weight G_s the dominant factor influencing the filtering effect. In edge regions, the pixel value weight G_r on the same side of the edge is similar and substantially larger (or smaller) than the G_r on the opposite side of the edge. In this scenario, the G_r on the opposite side has minimal impact on the filtering result, and the edge information is protected effectively, demonstrating good adaptability.

- 4) Finally, the processed sinograms can be reconstructed into images using the inverse Radon transform-based

CT backprojection methods, such as direct backprojection (DBP) and filtered backprojection (FBP)^[23].

3. Experiment

According to the configuration in Fig. 1, we experimentally established and conducted a photonic THz-CT system. To characterize the stability and estimate the noise of our system, we calculated the mean and standard deviation of the amplitude captured by the LIA over 24 h, as shown in Fig. 2. Please note that the system gradually stabilizes as thermal and environmental fluctuations decrease over time, leading to data stability improvement after 24 h. Previously, the smallest standard deviation of amplitude reported by us based on OFC was 0.032 mV^[13]. In this work, we enhanced the amplitude stability and achieved a standard deviation of 0.016 mV by removing the effects of secondary mixers. Moreover, the stability performance remained excellent after 24 h. Our system represented the lowest reported amplitude standard deviation above the 300 GHz band, and more detailed analysis on the THz OFC transmitter and its development have also been discussed in our previous work^[7].

To validate our proposed system and analyze the error, we first used two hex wrenches concealed within a shelter for detection. As depicted in Figs. 3(a) and 3(b), the spacings between the two hex wrenches were 15 mm in the vertical direction and 31 mm in the horizontal direction, respectively. We detected the targets for extensive experiments, and one representative set of the images using DBP and FBP is displayed in Figs. 3(c) and 3(d). Both hex wrenches were clearly visible in the images, with the FBP-based image exhibiting higher definition but larger background noise. The measured distances between the two targets were 15.5 mm in the vertical direction and 31.5 mm in the horizontal direction, slightly exceeding the actual measurements. This discrepancy was mainly attributed to the effects

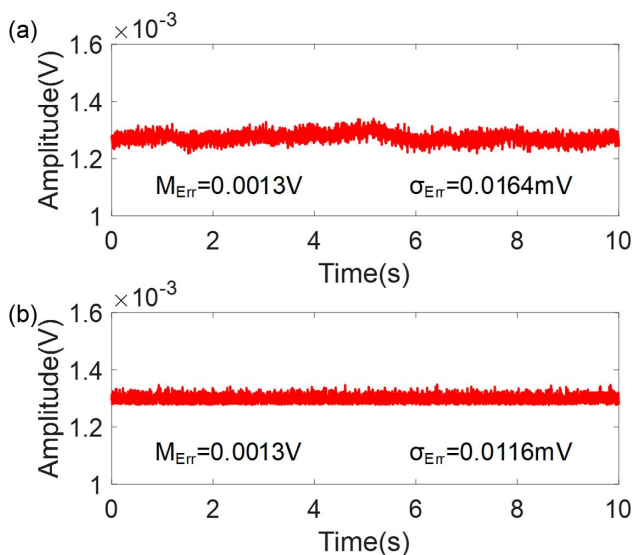


Fig. 2. Output of the LIA without a sample. (a) System just up and (b) running after 24 h.

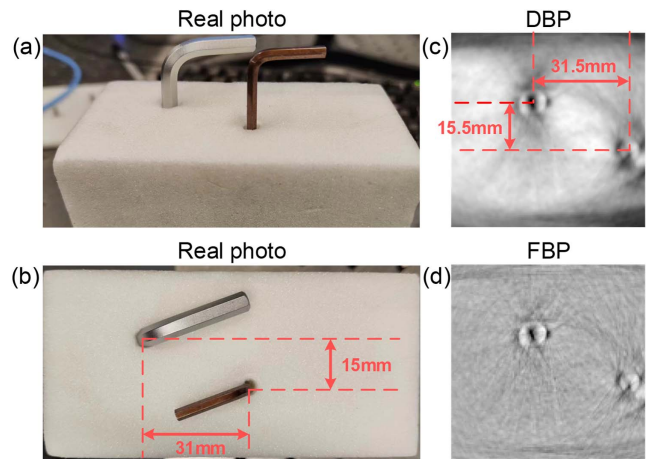


Fig. 3. (a), (b) Real photos of two hex wrenches concealed in a shelter; (c), (d) images based on DBP and FBP.

of the shelter, whose refractive index was higher than that of air, causing the THz beam to refract. Additionally, the vibration of the motors in motion may also contribute to the error.

4. Discussion

To further evaluate the performance of our imaging algorithms, we used a sample of the letter “J” made of polymer material concealed within a section of pipe, fixed on a platform, as depicted in Fig. 4(a). The sample is made by Sculpteo’s VeroWhite Resin material, with a permittivity of 2.72, and the pipes are standard plastic water pipes made of synthetic resin. We obtained images based on DBP and FBP directly from the original CT sinogram [Fig. 4(b)], as shown in Figs. 4(c) and 4(d). The letter appeared blurred, especially in the DBP scheme, and the FBP-based image had many messy lines, which seriously deteriorated the image quality.

Next, we applied our imaging algorithms to the original CT sinogram. After preprocessing, salt and pepper noise was effectively diminished, leading to a noticeable reduction in noise levels in the subsequent images. Applying sharpening enhanced the

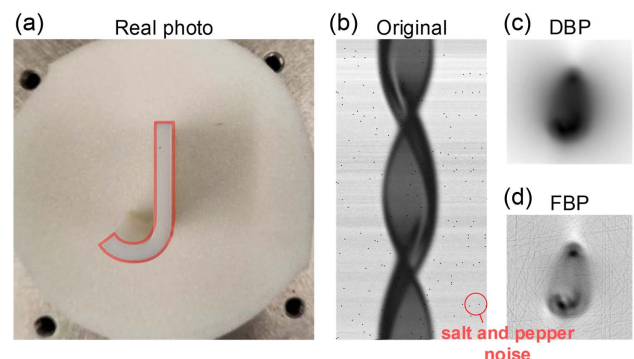


Fig. 4. (a) Real photo of sample J; (b) detected original CT sinogram; (c), (d) images based on DBP and FBP.

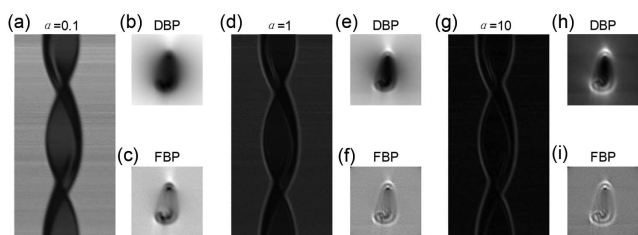


Fig. 5. The processed sinograms after sharpening with sharpening coefficients of (a) 0.1, (d) 1, and (g) 10; (b), (c), (e), (f), (h), (i) the images based on DBP and FBP corresponding to each sharpening coefficient.

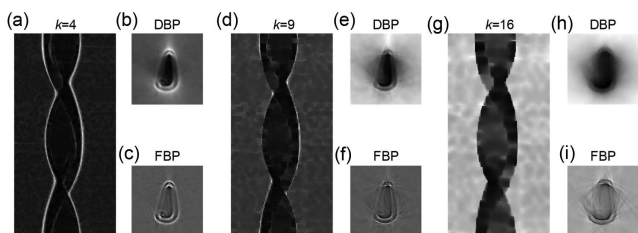


Fig. 6. The processed sinograms after bilateral filtering with filter windows of (a) 4, (d) 9, and (g) 16; (b), (c), (e), (f), (h), (i) the images based on DBP and FBP corresponding to each filter window.

clarity of edges, as displayed in Fig. 5. While there was an improvement in the imaging results, the extent of enhancement was constrained as the sharpening coefficient increased. Although the edges of the letter became clearer, the main body remained blurry. Subsequently, applying a bilateral filter filtered out noise except for the edges, as shown in Fig. 6. Different sizes of the filter window yielded different filtering effects. A small filter window made it challenging to distinguish between edge and flat regions, resulting in overly preserved edges; conversely, a large filter window tended to overlook subtle edge variations, leading to distortions in the imaging results.

To demonstrate the efficacy of our imaging algorithms, we detected and imaged samples featuring the letters “Z,” “J,” and “U,” with the results displayed in Fig. 7. The letters Z, J, and U were readily recognizable in the images based on DBP and FBP after processing with our specialized THz imaging algorithms. Compared to the images without processing, our imaging algorithms exhibited significant adaptability to both CT imaging schemes. However, there were still distortions at the head and tail of the letters, primarily caused by the scattering of the THz beam due to the corner angles of the samples. Addressing these distortions was crucial for further improving image quality. One potential solution to mitigate this issue was the application of axicon lenses, which can help tackle the scattering effects more effectively^[12].

5. Conclusion

In conclusion, we propose a photonic CW THz-CT system operating above 300 GHz. Utilizing an OFC and specialized THz

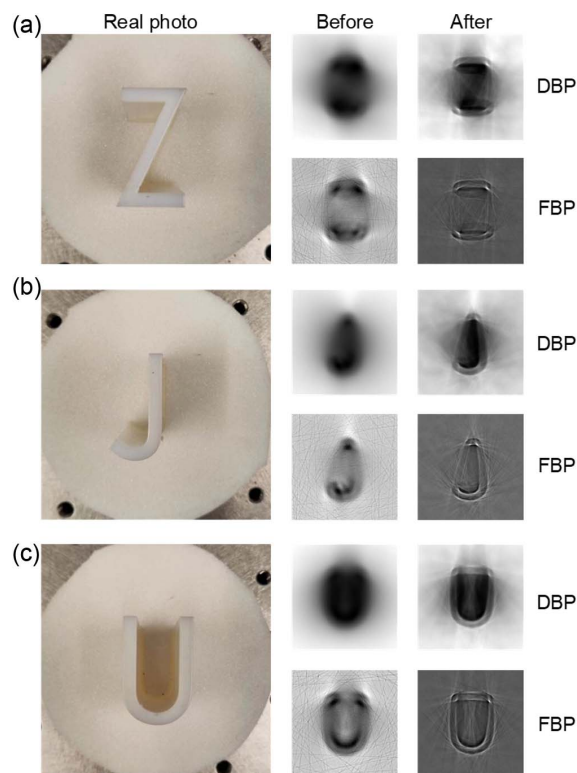


Fig. 7. The real photos of samples and imaging results of letters (a) Z, (b) J, and (c) U.

imaging algorithms, our system achieves flexible frequency tunability across a wide THz frequency range, which effectively reduces blur and distortion in detection. The experimental system demonstrates stable performance over 24 h, high resolution with a 0.5 mm error margin, as well as nondestructive CT imaging capability. We believe our system holds significant potential for various THz-CT applications, such as medical examination, food evaluation, and defect detection.

Acknowledgements

This work was supported by the National Key R&D Program of China (No. 2022YFB2903800), the “Pioneer” and “Leading Goose” R&D Program of Zhejiang (No. 2023C01139), and the National Natural Science Foundation of China (No. 62471433).

References

1. Y. B. Ji, S. J. Oh, S.-G. Kang, *et al.*, “Terahertz reflectometry imaging for low and high grade gliomas,” *Sci. Rep.* **6**, 36040 (2016).
2. E.-M. Stübling, A. Rehn, T. Siebrecht, *et al.*, “Application of a robotic THz imaging system for sub-surface analysis of ancient human remains,” *Sci. Rep.* **9**, 3390 (2019).
3. Y. Wang, H. Minamide, M. Tang, *et al.*, “Study of water concentration measurement in thin tissues with terahertz-wave parametric source,” *Opt. Express* **18**, 15504 (2010).

4. H. Song, S. Hwang, H. An, *et al.*, "Continuous-wave THz vector imaging system utilizing two-tone signal generation and self-mixing detection," *Opt. Express* **25**, 20718 (2017).
5. X. Cao, X. Gao, L. Zhang, *et al.*, "300 GHz vector imaging system based on self-mixing detection," in *Proc. SPIE* **11455**, 114557W (2020).
6. S. Dülme, M. Steeg, I. Mohammad, *et al.*, "Ultra-low phase-noise photonic terahertz imaging system based on two-tone square-law detection," *Opt. Express* **28**, 29631 (2020).
7. Z. Yang, L. Zhang, Z. Lu, *et al.*, "Robust photonic terahertz vector imaging scheme using an optical frequency comb," *J. Lightwave Technol.* **40**, 2717 (2022).
8. W.-T. Su, Y.-C. Hung, P.-J. Yu, *et al.*, "Physics-guided terahertz computational imaging: a tutorial on state-of-the-art techniques," *IEEE Signal Process. Mag.* **40**, 32 (2023).
9. S. Mou, A. D'Arco, L. Tomarchio, *et al.*, "Generation of terahertz vector beam bearing tailored topological charge," *APL Photonics* **8**, 036103 (2023).
10. L. Chen, Y. Wang, D. Xu, *et al.*, "Terahertz computed tomography of high-refractive-index objects based on refractive index matching," *IEEE Photonics J.* **10**, 5900813 (2018).
11. D. Wang, B. Li, L. Rong, *et al.*, "Extended depth of field in continuous-wave terahertz computed tomography based on Bessel beam," *Opt. Commun.* **432**, 20 (2019).
12. S. Shen, C. Hao, B. Liang, *et al.*, "Terahertz fan-beam computed tomography," *Opt. Lett.* **49**, 2481 (2024).
13. A. Duhant, M. Triki, and O. Strauss, "Terahertz differential computed tomography: a relevant nondestructive inspection application," *J. Infrared Millimeter Terahertz Waves* **40**, 178 (2019).
14. P. Fosodeder, S. Hubmer, A. Ploier, *et al.*, "Phase-contrast THz-CT for non-destructive testing," *Opt. Express* **29**, 15711 (2021).
15. D. Wang, R. Ning, G. Li, *et al.*, "3D image reconstruction of terahertz computed tomography at sparse angles by total variation minimization," *Appl. Opt.* **61**, B1 (2022).
16. P. Fosodeder, S. van Frank, and C. Rankl, "Highly accurate THz-CT including refraction effects," *Opt. Express* **30**, 3684 (2022).
17. T. Wang, K. Wang, K. Zou, *et al.*, "Virtual unrolling technology based on terahertz computed tomography," *Opt. Lasers Eng.* **151**, 106924 (2022).
18. H. Guerboukha, K. Nallappan, and M. Skorobogatiy, "Toward real-time terahertz imaging," *Adv. Opt. Photonics* **10**, 843 (2018).
19. H. Ito, S. Kodama, Y. Muramoto, *et al.*, "High-speed and high-output in-pi-ngaas unitraveling-carrier photodiodes," *IEEE J. Sel. Top. Quantum Electron.* **10**, 709 (2004).
20. N. Gallagher and G. Wise, "A theoretical analysis of the properties of median filters," *IEEE Trans. Acoust. Speech Signal Process.* **29**, 1136 (1981).
21. N. Kanopoulos, N. Vasanthavada, and R. L. Baker, "Design of an image edge detection filter using the sobel operator," *IEEE J. Solid-State Circuits* **23**, 358 (1988).
22. C. Tomasi and R. Manduchi, "Bilateral filtering for gray and color images," in *Sixth International Conference on Computer Vision (IEEE Cat. No. 98CH36271)* (1998), p. 839.
23. M. J. Willeminck and P. B. Noël, "The evolution of image reconstruction for ct-from filtered back projection to artificial intelligence," in *Eur. Radiol.* **29**, 2185 (2019).